RSC Advances

ROYAL SOCIETY OF CHEMISTRY

www.rsc.org/advances

Journal Name

ARTICLE

In Situ Ion-Exchange Synthesis of SnS_2/g-C_3N_4 Nanosheets Heterojunction for Enhancing Photocatalytic Activity

Received 18th september 2015,
Accepted 00th January 20xx

DOI: 10.1039/x0xx00000x

www.rsc.org/

Yongping Liu [a,b], Peng Chen[b], Yuan Chen[b], Huidan Lu*[,a,b], Jixiang Wang[b], Zhishu Yang[b], Zhenhuan Lu*[, a,b], Ming Li[a,b], and Liang Fang[c]

In this paper, free standing graphitic carbon nitride (g-C_3N_4) nanosheets have been synthesized by mixed solvents (water/ IPA = 2/1) liquid phase exfoliation, and a series of SnS_2/ g-C_3N_4 heterojunctions with different contents of SnS_2 have been prepared via a simple ion-exchange process. Exfoliated g-C_3N_4 presents a two-dimension sheet-like structure with the thickness of 2.8 nm and small SnS_2 nanoparticles with diameter of 5-10 nm are well anchored on the surface of g-C_3N_4 nanosheets, which was proved by transmission electron microscopy (TEM) and atomic force microscope (AFM). The 4.0-SnS_2/g-C_3N_4 sample shows the highest photocurrent density of 13.66 μA/cm^2 at 0.8 V, which is about 1.5 time of the g-C_3N_4 nanosheets and 2 times of the bulk g-C_3N_4, respectively. Photocatalytic measurement also demonstrated that constructing heterojunction of SnS_2/g-C_3N_4 can improve the photocatalytic efficiency as compared to pure g-C_3N_4 and g-C_3N_4 nanosheets. The highly effective photoelectrochemical and phocatalytic activities of SnS_2/g-C_3N_4 heterojunctions are attributed to the efficient separation of photogenerated hole-electron pairs. This work may provide a novel concept for the rational design of high performance g-C_3N_4-based photocatalysts.

1. Introduction

Semiconductor photocatalysis is regarded as an effective and green technique since it is able to decompose a variety of environmental contaminations under mild conditions [1-3]. Over the past several years, graphite carbon nitride (g-C_3N_4) has attracted considerable attention owing to its photocatalytic properties, as well as its promising applications in the fields of catalysis, photoelectron apparatus and chemical sensors. The high chemical stability and desirable band gap (2.7 eV) of g-C_3N_4 make it an exceptionally promising organic semiconductor photocatalyst for water splitting and degradation of pollutant [4, 5]. Wang et al. first reported that g-C_3N_4 can catalyze water splitting and produce the hydrogen in visible light [5]; Zou et al. confirmed that g-C_3N_4 can oxidize the organic pollution under visible light irradiation, thus achieve the goal of dispelling the pollutant[6].

However, the photocatalytic activity of pure g-C_3N_4 is low owing to its poor light-absorbance and fast recombination of photo-generated electron-hole pairs[6]. Recent investigations show that single or several atom thickness g-C_3N_4 nanosheets have improved photocatalytic property, strong electrochemical luminescence activity, good biocompatibility and high fluorescent quantum yield compared with their bulk counterparts [7-9]. Usually, g-C_3N_4 nanosheets are prepared by liquid phase separation method in water or organic solvent by ultrasonic exfoliating process [7, 10, 11]. Zhao et al. prepared single atomic layer of g-C_3N_4 nanosheet and adopt it for degradation Rhodamine B [12], as a result, they found that the photocatalytical activity of single layer graphitic g-C_3N_4 was about 3 and 10 times higher than that of few layer g-C_3N_4 and bulk g-C_3N_4.

Constructing heterconjection is another way to improve the photocatalytic performance of C_3N_4. Among various carbon nitride crystal forms, g-C_3N_4 possesses the smallest band gap, so it is easy to form a heterojunction[13, 14], for instance ZnO/g-C_3N_4[15], Bi_2WO_6/g-C_3N_4[16], g-C_3N_4/TiO_2[17] and g-C_3N_4/$SrTiO_3$[18]. Katsumata et al. prepared the g-C_3N_4/Ag_3PO_4 heterojunction with different weight ratios of g-C_3N_4 by a facile in situ precipitation method, which showed highly effective photocatalytic activity under visible light irradiation. Hou et al. constructed 2D porous graphitic C_3N_4 nanosheets/nitrogen-doped graphene/layered MoS_2 ternary nanojunction[19]. Chen et al. used ion exchange process to prepare the g-C_3N_4/NiS composite material and found that the sample containing 1.5 % NiS exhibited the highly photocatalytic activity[20]; Young-Si Jun et al. adopt a new approach to assemble low-dimensional g-C_3N_4 into a three-dimensional structure, which significantly improved photocatalytic properties [21].

[a] Guangxi Key Laboratory of Electrochemical and Magneto-chemical Functional Materials, Guilin University of Technology, Guilin, P.R. China.
Email: E-mail: lhuidangl@163.com, zhenhuanlu@glut.edu.cn
[b] College of Chemistry and Bioengineering, Guilin University of Technology, Guilin, P.R. China.
[c] State Key Laboratory Breeding Base of Nonferrous Metals and Specific Materials Processing, Guilin University of Technology, Guilin 541004, P.R. China.
† Footnotes relating to the title and/or authors should appear here.
Electronic Supplementary Information (ESI) available: [details of any supplementary information available should be included here]. See DOI: 10.1039/x0xx00000x

SnS_2 is a nontoxic and low-priced semiconductor material with a visible-light band gap of 2.2-2.35 eV. So, we choose SnS_2 to form heterconjections with few layer g-C_3N_4 nanosheets for increasing photon-generated carrier transfer. In this paper, we have prepared free standing g-C_3N_4 nanosheets by liquid phase exfoliation, and successfully synthesized SnS_2/g-C_3N_4 nanosheet heterojunction via a simple ion-exchange process. Moreover, we explored the photoelectrochemical response and photocatalytic performance of SnS_2/g-C_3N_4 heterojunction, which exhibited the higher photocurrent and photocatalytic efficiency compared with pure g-C_3N_4 nanosheets. Additionally, a smaller charge transfer resistance was observed for the heterojunction under visible light irradiation.

2. Experimental section

2.1 Preparation of photocatalysts

All reagents were analytical grade and purchased from Shanghai Reagents Company (Shanghai, China). The bulk g-C_3N_4 was synthesized by polymerization of melamine molecules under high temperature. In brief, 3 g melamine was added in a crucible with a cover and heated at 500 ℃ for 2 h under air atmosphere with a ramp rate of about 10 ℃/min, then heated at 520 ℃ for 2 h with a ramp rate of 5 ℃/min. After cooling to room temperature, the obtained yellow product was the g-C_3N_4 powder.

The g-C_3N_4 nanosheets were obtained by liquid exfoliation of as-prepared bulk g-C_3N_4 in various solvents via sonication. Typically, 20 mg of bulk g-C_3N_4 was added into 20 mL flask with 15 mL different solvents such as isopropyl alcohol (IPA), water, ethanol, formamide, N-methyl-pyrrolidone (NMP), or the mixture solvents (water and IPA). Then, the flask was ultrasounded for 10 h. The initial formed suspension was centrifuged at about 3000 rpm to remove aggregates, and then, the supernatant was collected, the exfoliated g-C_3N_4 nanosheets were obtained, centrifuged and dried in vacuum for further characterization.

The SnS_2/g-C_3N_4 heterjunctions were prepared through an ion-exchange method at room temperature, as shown in Scheme 1. Firstly, 30, 60, 90 or 120 μL of 0.01 M $SnCl_4$ solution was dropped in the 10 mL g-C_3N_4 nanosheets dispersion (a concentration of 0.27 mg/mL). After stirring 20min, 60, 120, 180 or 240 μL of 0.01 M Na_2S solution was added into the above mixed dispersion. The mixed solution was stirred for another 5 minutes, then the solution was centrifuged at 14000 rpm for 10 min, and the precipitates were collected and washed with ethanol and deionized water 3 times, respectively. The products were dried for 12 h in a vacuum oven at 80 ℃. The mass ratio of SnS_2 to g-C_3N_4 nanosheets are 2%, 4%, 6%, and 8 % in the final samples, thus they are denoted as 2.0-SnS_2/g-C_3N_4, 4.0-SnS_2/g-C_3N_4, 6.0-SnS_2/g-C_3N_4 and 8.0-SnS_2/g-C_3N_4, respectively.

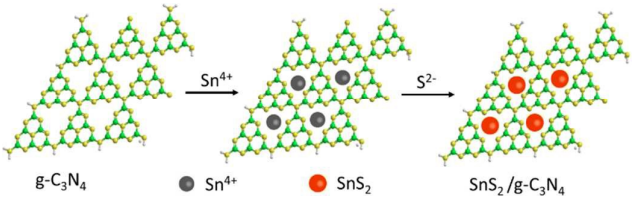

Scheme 1. Schematic representation of the deposition of SnS_2 nanoparticles on g-C_3N_4 sheets.

Bulk SnS_2 were synthesized by precipitation method. Briefly, 20mL of 0.01M $SnCl_4$ solution was dropped in 50mL of 0.01 M Na_2S solution and the mixed solution was stirred for 30 minutes, then the precipitate was collected by centrifuged.

2.2 Characterization

The crystal structures of the as-synthesized samples were characterized by PANalytical X'Pert PRO X-ray diffraction (XRD) with CuKα radiation (λ=1.54 Å) in the range of 10 to 80°. Fourier transform infrared (FT-IR) spectra were obtained on a fourier transform infrared spectroscopy (Nicolet iS10, Thermo Fisher). The microstructures of the as-prepared samples were characterized by the transmission electron microscopy (TEM, JEOL, JEM-2100F) and atomic force microscope (AFM, NT-MDT, Ntegra Prima SPM). The diffuse reflectance spectra (DRS) of the as-obtained samples were measured by a UV/VIS/NIR Spectrometer (PerKinElmer, Lambda 750) in the range of 200 to 1100 nm. $BaSO_4$ was used as the reflectance standard material. The X-ray Photoelectron Spectroscopy (XPS) were taken by ESCALAB 250Xi system (Thermo Electron Corporation, USA). The excitation source was AlKα radiation (photoelectron energy of 1253.6 eV). Survey scans and relevant core levels were recorded: Sn 3d, S 2p, C 1s and N 1s.

2 .3 Photoelectrochemical and photocatalytic measurement.

Photoelectrochemical measurements were performed on a conventional three-electrode cell under dark and simulated sunlight irradiation (350 W Xe lamp, a cutoff filter of 420 nm). The samples of the above were spin-dropped on the 1 cm × 1 cm indium tin oxide (ITO) glass at 600 rpm for 30 s, and then dried at 60 ℃ for 1 h for obtaining working electrodes with a similar film thickness. Pt wire worked as the counter electrode and Ag/AgCl electrode as the reference electrode and 0.2 M Na_2SO_4 solution was used as the electrolyte. For Nyquist plots measurements, the perturbation signal was 20 mV and the frequency ranged from 100 kHz to 10 mHz.

The photocatalytic activity of powder samples was evaluated by the degradation of methyl orange (MO) The optical system for the degradation reaction included a 350 W Xe lamp, a cutoff filter of 420 nm. In each experiment, 20 mg photocatalyst was added to 100 mL dye aqueous solution (10mg L^{-1}). Before irradiation, the suspensions were magnetically stirred in the dark for 30 min to ensure the establishment of an adsorption/desorption equilibrium between the photocatalyst and the dye. During the reaction process under visible light illumination, 3 mL of suspension

was sampled at given time intervals and centrifuged to remove the photocatalyst particles. The concentration of MO was determined by monitoring the height of the maximum of the absorbance in ultraviolet-visible spectra.

To explore the photo-induced radical species in the photocatalytic degradation of MO, the reactive species trapping experiments were performed. The benzoquinone and IPA were utilized as the scavenger of the superoxide radical ($\cdot O_2^-$) and hydroxyl ($\cdot$OH), respectively. For the h^+ hole, disodium ethylenediaminetetraacetate (EDTA-2Na) was used as quencher. The trapping experiment taken was similar to the above photocatalytic activity test except that the different scavengers were added into the MO solution.

3. Results and Discussion.

Bulk g-C_3N_4 was suspended in various solvents such as IPA, NMP, water, ethanol, and formamide to create light yellow dispersions with the same concentration of 2 mg·mL^{-1}, and then sonicated at room temperature for the gradual exfoliation of bulk g-C_3N_4 to nanosheets (As illustrated in Fig. S1). Similar method is used to exfoliate various layered materials, such as boron nitride [22], MoS_2 [23, 24], to single or few-layers nanosheets via the interaction of solvent molecules. Liquid exfoliation effect is significantly influenced by the surface energies of used solvents. Organic molecules could be similarly inserted into layers of the bulk material and generate interaction when surface energy matching. As a result, layer material was gradually exfoliated to single-or few-layer nanosheets. From Fig. S1, it can be seen that g-C_3N_4 nanosheets can be well dispersed in water, isopropyl alcohol and NMP. Although g-C_3N_4 nanosheets easily disperse in water, it is not stable and tends to sedimentation. While, g-C_3N_4 nanosheets were very stably disperse in IPA (shown in Fig. S2) just with a low yield after sonication. Meanwhile, NMP has the high boiling point, so it was difficult to remove. Thus, we choose the mixed solvents of water and isopropyl alcohol as a dispersant. From Fig. 1, it is observed that g-C_3N_4 nanosheets concentration in the solvent is gradually decreased with the reduction of the amount of water. The prepared g-C_3N_4 nanosheets have a relatively high concentration and a better stability when the volume ratio of water and IPA is 2:1 (As illustrated Fig. S2). Therefore, we exfoliated bulk g-C_3N_4 for ensure the stability and dispersion using the mixed solvents of water and IPA with volume ratio of 2:1.

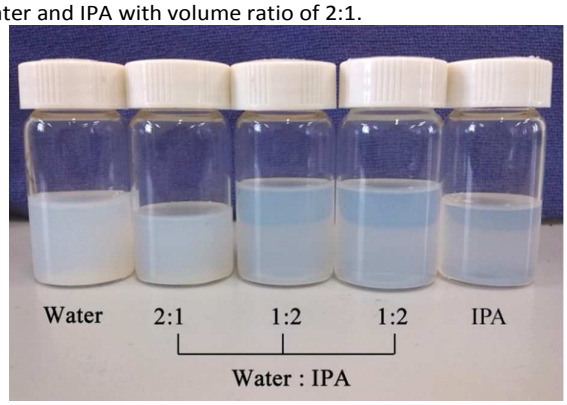

Fig. 1 Photographs of the dispersions of g-C_3N_4 nanosheets in water, IPA, and the mixture.

The crystal structure of the obtained samples was investigated by X-ray diffraction (XRD). As seen clearly from Fig. 2, the pure g-C_3N_4 nanosheets and SnS_2/g-C_3N_4 heterojunction have two distinct diffraction peaks at 27.5° and 13.2°, which can be indexed for graphite-like materials as the (002) and (100) diffraction plane. The (002) peak at 27.5° and the (100) peak at 13.2°corresponding to distance of 0.324 and 0.670 nm reflects the characteristic inter-planar stacking peak of conjugated aromatic systems and in-plane structural packing motif, respectively[25]. In addition, the characteristic diffraction peaks of SnS_2 appear at 51.8°. Seen from the illustration of Fig. 2, the diffraction peak at 51.8° gradually increase with the increasing amount of SnS_2 for SnS_2/g-C_3N_4 heterojunctions.

The atomic structure of bulk g-C_3N_4 and g-C_3N_4 nanosheets were characterized by FT-IR spectroscopy. As shown in Fig. 3, the absorption band of 3000~3600cm^{-1} is due to NH stretching vibration mode, and absorption band of 1200 ~1700 cm^{-1} is ascribed to the stretching vibration mode of CN hetero-ring[26]. Note that, strong absorption peak at 809 cm^{-1} is the bending vibration peak of the s-triazine ring[27]. In the case of SnS_2 nanosheets, a broadband peaked at 545 cm^{-1} is originated to the vibration of Sn-S bands[28]. However, this feature band is difficult to distinguish on the curve of SnS_2/g-C_3N_4 heterojunction nanosheets due to the low content of SnS_2 nanoparticle.

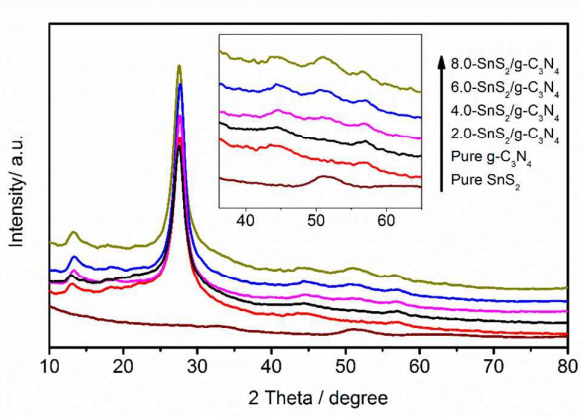

Fig. 2 XRD patterns of pure g-C_3N_4, pure SnS_2 and SnS_2/g-C_3N_4.

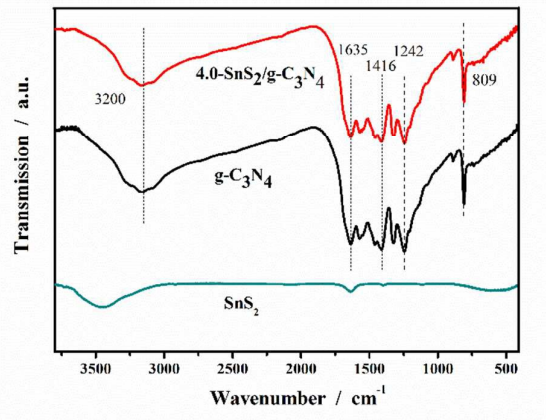

Fig. 3 FT-IR spectra of bulk g-C_3N_4 and g-C_3N_4 nanosheets.

The chemical compositions of the as-prepared photocatalysts are characterized by XPS spectra, as shown in Fig. 4. The appearance of elements Sn, S, C, N in survey XPS spectrum of 4.0-SnS_2/g-C_3N_4 hybrid confirms the presence of both components C_3N_4 and SnS_2, as shown in Fig. 4a. The high-resolution spectrum of C1s (Fig. 4b) can be deconvoluted into three peaks at 284.6 eV, 285.8 eV and 288.1 eV, corresponding to sp^2-bonded aromatic structure (N-C=N), graphitic carbon (C-C), and residual C–O, respectively [10, 29]. As to the N1s spectrum of g-C_3N_4 nanosheets (Fig. 4c), N1s peak at 398.5 eV corresponds to sp2 hybridized aromatic N bonded to carbon atoms (C = N–C). The peak at 399.56 eV is assigned to the tertiary N bonded to carbon atoms in the form of N–$(C)_3$ or H–N–$(C)_2$. The weaker peak with a high binding energy at 400.9 eV is attributed to quaternary N bonded to three carbon atoms in the aromatic cycles and the peak centered at 404.3 eV

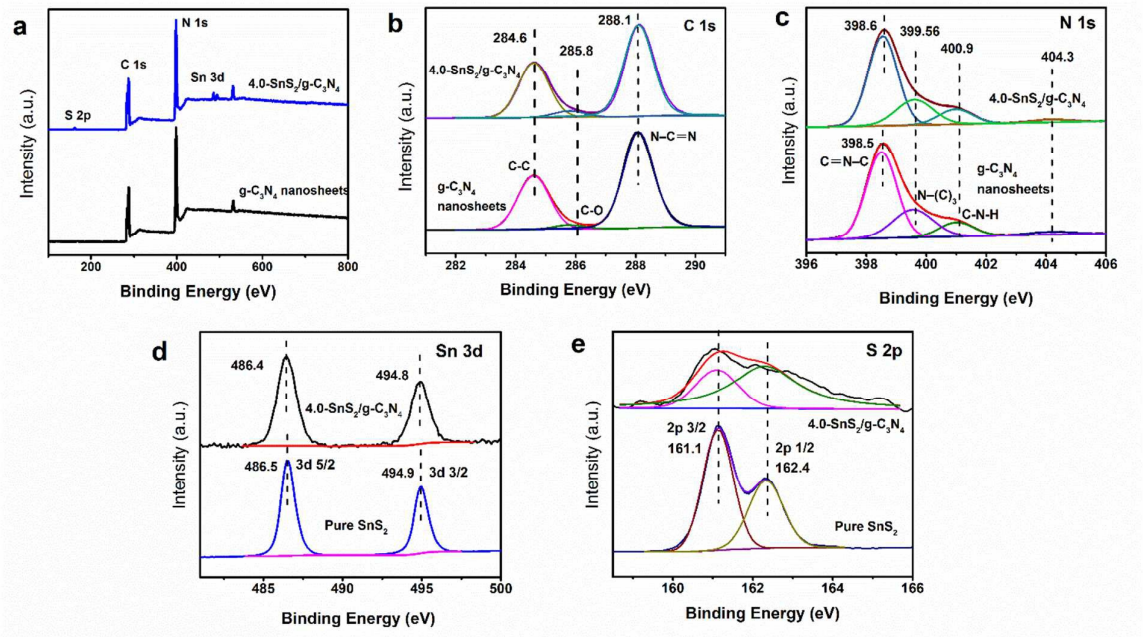

Fig. 4 XPS survey spectrum(a), high resolution of C 1s (b), N 1s (b), Sn 3d (c), S 2p (d) spectra of as-prepared photocatalysts.

correspondes to the π excitations [30, 31]. The evolution of Sn 3d with two strong peaks is observed at 486.5 and 494.9 eV(Fig. 4d), which were attributed to Sn 3d5/2 and Sn 3d3/2, respectively [32]. However, the peak relating to the C= N-C bonds of g-C_3N_4 nanosheets is shifted slightly to the higher binding energy side after loading SnS_2 and the S 2p peaks of SnS_2, reflecting to S-Sn bond [32], are also moved to the low binding energy side, when coupling with g-C_3N_4 nanosheets. It is indicated that there might be some interactions between the "nitrogen pots" of g-C_3N_4 with the Sn species of SnS_2.The observed binding energies of Sn 3d and S 2p spectra are in good accordance with Sn^{4+} and S^{2-} of SnS_2.

TEM image of the g-C_3N_4 nanosheets (Fig. 5c) clearly presents a two-dimension sheet-like structure with relatively smooth surface. For revealing microstructures and the thickness, the diluted dispersion of the products obtained after ultrasonication treatment of bulk g-C_3N_4 was further investigated by AFM analyses. The AFM image (Fig. 5a) shows the exfoliated products are free-standing nanosheets with a large lateral size of 300–400 nm. Fig.5b presents the thickness of the products is about 2.8 nm, suggesting 8-9 atomic monolayers [33, 34]. In addition, the exfoliated sample can be formed to stable colloidal dispersion over a period of two weeks and exhibits a typical Tyndall effect. The TEM image of SnS_2/g-C_3N_4 hybrid is displayed in Fig. 5d, which shows that some small SnS_2 nanoparticles with diameter of 5-10 nm are well anchored on the surface of g-C_3N_4 nanosheets. These results indicated that SnS_2 has combined with ultrathin g-C_3N_4 nanosheets to form effective SnS_2/g-C_3N_4 heterojunction.

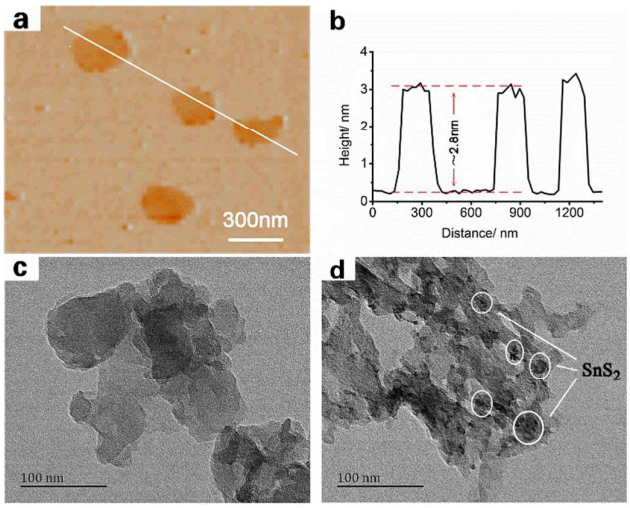

Fig. 5 AFM image (a) and the corresponding height analyses of g-C_3N_4 nanosheets (b), the TEM image of the g-C_3N_4 nanosheets (c) and the SnS_2/g-C_3N_4 hybrid (d).

The UV–vis diffuse reflection spectra of the SnS_2/g-C_3N_4 hybrids with different mass percentage of SnS_2, together with those of pure g-C_3N_4 nanosheets and pure SnS_2, were investigated and shown in Fig. 6a. The pure g-C_3N_4 nanosheets show an absorption edge at 450 nm, corresponding to band gap of ~2.65 eV presented in Fig. 6b, and it is well be in consistent with the value of previously reported literature[35, 36]. The pure SnS_2 displays light absorption over nearly entire visible light range. After introducing SnS_2, the SnS_2/g-C_3N_4 samples show the similar absorption edge and a broader absorption in the visible region as comparison to pure g-C_3N_4 nanosheets. Moreover, the absorption intensity of SnS_2/g-C_3N_4 samples in the visible region is gradually strengthened with increasing SnS_2 contents.

The band gap energy of the semiconductors can be calculated by the following equation[38,39]:

$$\alpha h\nu = A(h\nu - E_g)^{n/2} \quad (1)$$

by applying the above equation, the band gaps of g-C_3N_4 and SnS_2 are 2.65 and 2.23 eV, respectively. It accords with the previous literatures very much[35,36,40-44].

The band edge positions of CB and VB for semiconductor can be determined by the following equations[44-46]:

$$E_{VB} = X - E_e + 0.5E_g \quad (2)$$

$$E_{CB} = E_{VB} - E_g \quad (3)$$

where E_{VB} is the VB edge potential, X is the electronegativity of the semiconductor, E_e is the energy of free electrons (4.5 eV on the hydrogen scale), and E_g is the band gap energy of the semiconductor calculated from the DR-UV-vis spectra. The conduction band edge potential (E_{CB}) was acquired using the equation (3). After calculation, it is known that the E_{CB} of g-C_3N_4 and SnS_2 are -1.09 and -0.14 eV, respectively. Then, the E_{VB} of g-C_3N_4 and SnS_2 are 1.56 and 2.09 eV, respectively. These results are very close to the reported values[39, 41, 44, 47].

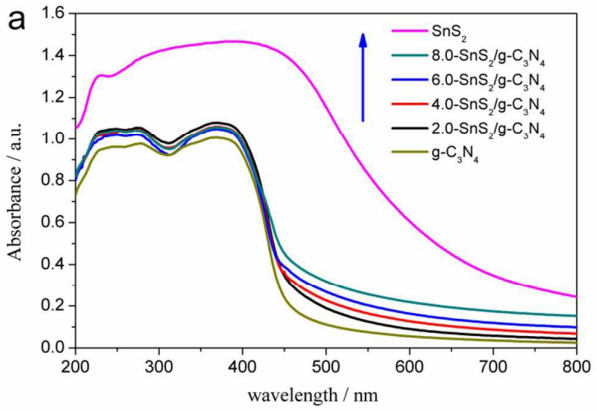

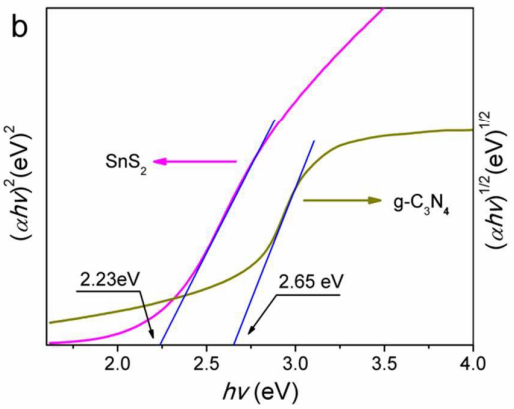

Fig. 6 (a) UV-vis diffuse reflection spectra of pure g-C_3N_4 nanosheets, pure SnS_2 and SnS_2/g-C_3N_4 heterojunctions; (b) band gap energies of SnS_2 and g-C_3N_4 nanosheets.

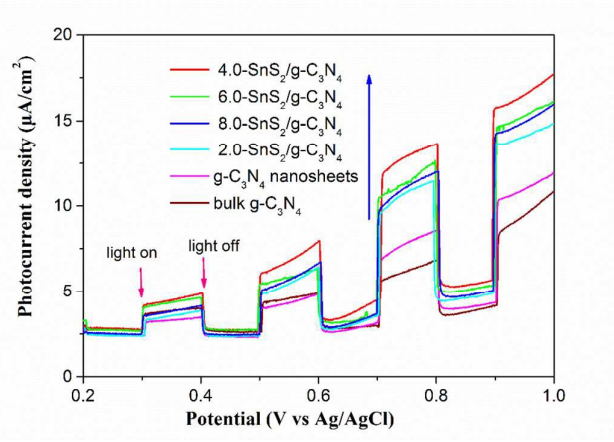

Fig. 7 Current-potential plots for bulk g-C_3N_4, pure g-C_3N_4 nanosheets and SnS_2/g-C_3N_4 hybrids under light switch.

To investigate photoelectrochemical performance of SnS_2/g-C_3N_4 heterojunction, typical current-voltage measurements of various samples were performed under light switch (Fig. 7). The 4.0-SnS_2/g-C_3N_4 heterojunction shows the highest photocurrent density of 13.66 μA cm^{-2} at 0.8 V, which is about 1.5 and 2 times of g-C_3N_4 nanosheets (9.02 μA cm^{-2}) and bulk g-C_3N_4 (6.82 μA cm^{-2}), respectively.

To gain deeper insights into the charge transport behavior in the system, we conducted electrochemical impedance spectroscopy (EIS) measurements (Fig. 8). In the Nyquist diagram, the radius of each arc is associated with the charge-transfer process at the corresponding electrode/electrolyte interface, and a smaller radius corresponds to a lower charge-transfer resistance. In Figure 8a, the impedance of the g-C_3N_4 nanosheets is significantly lower than the bulk material, and when the light source turned on, the impedance is further reduced, which also confirms that the g-C_3N_4 nanosheets has better photoelectric properties. Obviously, the 4.0-SnS_2/g-C_3N_4 heterojunction exhibits minimal charge transfer resistance under simulated sunlight irradiation, indicating that effective shuttling of charges between the electrode and the electrolyte. Faster interfacial charges transfer occurred at composite interface, thereby generating the increasing photocurrent. So, SnS_2 may serve as electron capture centres, speeding up charges transfer.

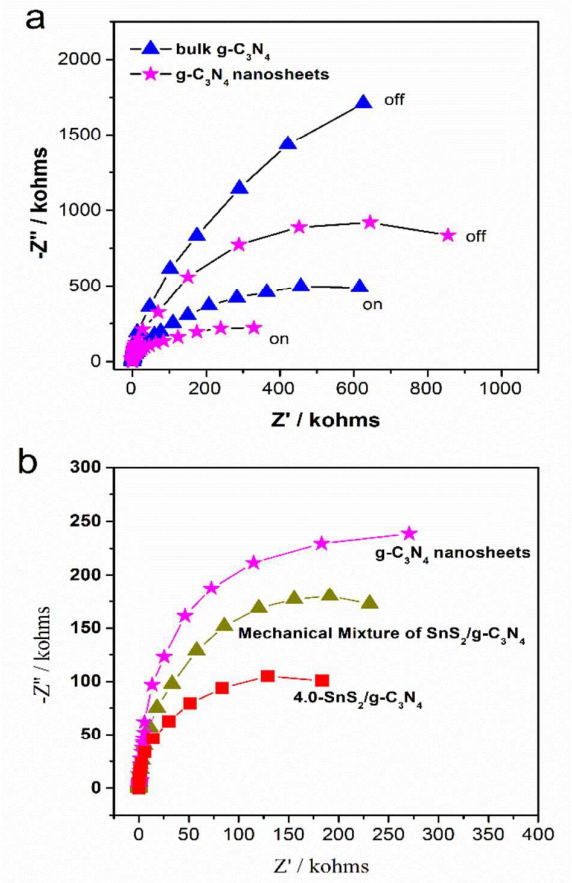

Fig. 8 (a) EIS Nyquist plots of the bulk g-C_3N_4, pure g-C_3N_4 nanosheets at a bias of 0.5V under dark and simulated sunlight irradiation. (b) EIS Nyquist plots of pure g-C_3N_4 nanosheets, mechanical mixture of SnS_2/g-C_3N_4 and 4.0-SnS_2/g-C_3N_4 at a bias of 0.5V under simulated sunlight irradiation.

Fig. 9a shows a comparison of the visible light photocatalytic activity of bulk g-C_3N_4, SnS_2 nanoparticles, g-C_3N_4 nanosheets and SnS_2/g-C_3N_4 composites. Prior to irradiation, the MO solution containing the catalyst was kept in the dark for 30 min to reach an adsorption/desorption equilibrium. As we can see, with absence of any photocatalyst the decompositon of MO hardly occurred when subjected to visible light irradiation. It is also suggested that the SnS_2 nanoparticles content has a significant effect on the photocatalytic activity of g-C_3N_4 nanosheets. In the case of bulk C_3N_4, approximately 82.6% of MO was decomposed after visible light irradiation for 40 min. When it comes to the pure g-C_3N_4 nanosheets, the degradation rate of MO is 90.7% and higher than that of SnS_2 nanoparticles which only display only 87.4% after irradiation for 40 min. However, the photoactivities of g-C_3N_4 nanosheets are obviously enhanced with the presence of SnS_2 nanoparticles on its surface. The photoactivities of SnS_2/g-C_3N_4 heterojunctions are higher than that of g-C_3N_4 nanosheets and SnS_2 nanoparticles. Especially, 4.0-SnS_2/g-C_3N_4, can decompose 95.3% of MO after only 25 min for visible light irradiation. The average decomposition rate of the MO dye over bulk g-C_3N_4, SnS_2 nanoparticles, g-C_3N_4 nanosheets and 4.0-SnS_2/g-C_3N_4 heterojunction is estimated to be about 0.0135 mg·min^{-1}, 0.0166 mg·min^{-1}, 0.0200 mg·min^{-1} and 0.0324 mg·min^{-1}. It reveals that constructing heterojunction of SnS_2/g-C_3N_4 could improve the photocatalytic efficiency of g-C_3N_4 nanosheets.

The reusability and stability of SnS_2/g-C_3N_4 heterojuncton was evaluated by recycling experiments. By utilizing the same photocatalyst and a fresh MO solution, five consecutive cyclic photodegradation experiments were carried out for the 4.0-SnS_2/g-C_3N_4 heterojunction. As shown in Fig. 9b, MO was decomposed and decreased in every cycling run. The percentage of degradation of MO after the first cycle was 94.9% by 25 min visible light irradiation; while it was 89.9% at the fifth cycle with the same time irradiation. Only a little decrease in catalytic activity was observed after the fifth-cycle decomposition process. So SnS_2/g-C_3N_4 nanosheets heterojunction could be regarded as a stable and durable photocatalyst.

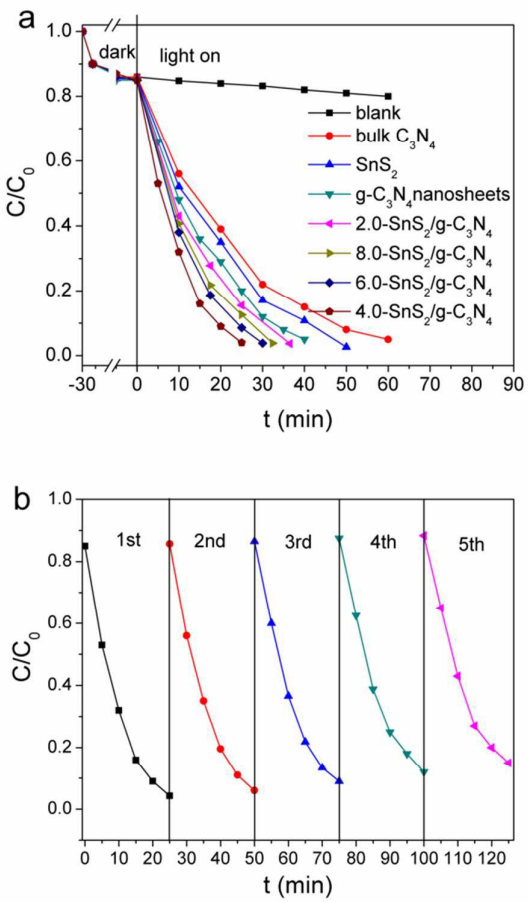

Fig. 9 (a) Photocatalytic degradation of MO with various powder samples, (b) the cycling runs of 4.0-SnS_2/g-C_3N_4 heterojunction for the photodegradation of MO under visible light.

It is well known that the $\cdot O_2^-$, ·OH and h^+ are the major reactive species for the photocatalytic decomposition. To uncover the possible photocatalytic mechanism of 4.0-SnS_2/g-C_3N_4 nanosheets heterojunction, the radical species trapping experiments were carried out to explore the main reactive species in the process of photocatalytic degradation. Herein, three chemicals including benzoquinone (BQ), disodium ethylenediaminetetraacetate (EDTA-2Na) and isopropyl alcohol (IPA) were utilized as the scavenger of $\cdot O_2^-$, h^+ holes and ·OH, respectively. As listed in Fig. 10a, the degradation efficiency of MO is 95% with absence of scavenger. When the IPA was added into the reaction solution, the degradation efficiency of MO is down to 73.5%. And adding the EDTA-2Na into the reaction solution, the degradation efficiency of MO is decreased to 43%. The degradation efficiency of MO is even whittled down into 28% with the presence of BQ. The phenomenon suggested that the photocatalytic activity of 4.0-SnS_2/g-C_3N_4 is extremely suppressed by BQ and EDTA-2Na, while slightly inhibited by IPA. It also can be concluded that $\cdot O_2^-$, ·OH and h^+ are the major reactive species for the 4.0-SnS_2/g-C_3N_4 nanosheets photocatalyst. The influencing degree is belonged to $\cdot O_2^- > h^+ > \cdot OH$.

On the basis of radical species trapping experiments and the aforementioned band gap energy analysis, the possible photocatalytic mechanism is speculated. As illustrated in Fig. 10b, the g-C_3N_4 nanosheets and SnS_2 semiconductor possess overlapping band potentials, indicating that the band potentials of g-C_3N_4 nanosheets and SnS_2 nanoparticles can be well matched to form an effective heterojunction. Under visible light irradiation, both components are readily excited to generate photo-induced electrons-holes pairs. And the separation process of photo-induced electrons-holes can be vividly described in Fig. 10b. When the SnS_2/g-C_3N_4 nanosheets heterojunctions absorb the visible light and then are excited, the quick and strong combination is occurred between the photo-induced electrons in the conduction band (CB) of SnS_2 and photo-induced holes in the valence band (VB) of g-C_3N_4 nanosheets. Meanwhile, the photo-induced electrons in the CB of g-C_3N_4 nanosheets, which have more negative potential than the standard redox potential of $E^o(O_2/\cdot O_2^-)$ = -0.33 eV (vs. NHE), can react with the O_2 to produce $\cdot O_2^-$. And then the generated holes in the VB of SnS_2 can directly decompose the MO molecules. Moreover, the generated holes in the VB of SnS_2, which have more positive potential than the standard redox potential of $E^o(\cdot OH/OH^-)$ = 1.99 eV (vs. NHE)[48-52], can oxidize OH^- to yield ·OH radicals. Therefore, a typical Z-scheme separation mechanism of photo-induced electrons-holes pairs is proposed and favourable for the generation of $\cdot O_2^-$ and ·OH reactive species. As a result, efficient separation of photo-generated hole-electron pairs is achieved by the distribution of electrons and holes on different semiconductors, thus enhance the corresponding photocatalytic performance.

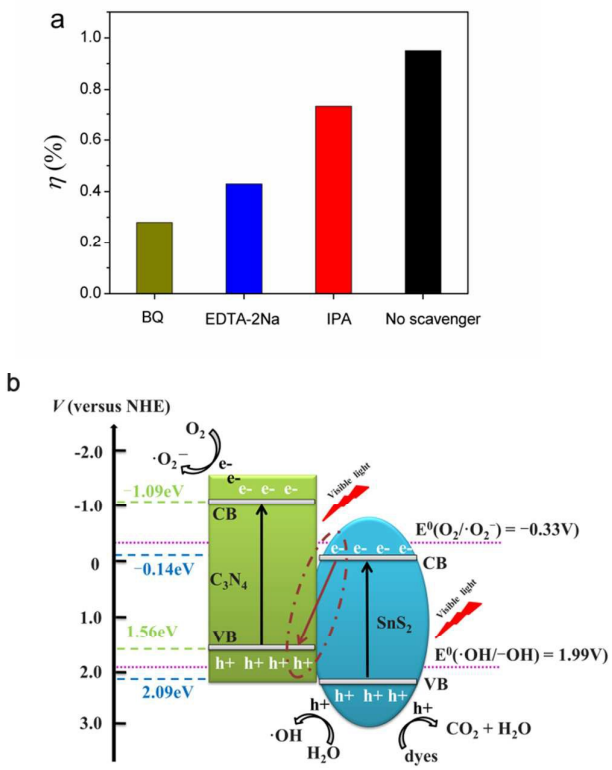

Fig. 10 (a) Effects of various scavengers on the photocatalytic efficiency of 4.0-SnS_2/g-C_3N_4 heterojuncton, (b) schematic model of the photocatalytic mechanism for SnS_2/g-C_3N_4 heterojunction.

4. Conclusions

In summary, we have prepared free standing g-C_3N_4 nanosheets by mixed solvents exfoliation and subsequently obtained SnS_2/g-C_3N_4 heterojunction via a simple ion-exchange process. It was observed that small SnS_2 nanoparticles with diameter of 5-10 nm are well anchored on the surface of g-C_3N_4 nanosheets. Photoelectrochemical and photocatalytic measurement proved that constructing heterojunction of SnS_2/g-C_3N_4 could significantly improve the photoelectochemical performance and photocatalytic efficiency as compared to pure g-C_3N_4 and g-C_3N_4 nanosheets. The highly effective photoelectron-chemical activities of g-C_3N_4/SnS_2 are attributed to the efficient separation of photo-generated hole-electron pairs on different semiconductors. Our findings pave the way to build the SnS_2/g-C_3N_4 heterojunction materials for photoelectrochemical application.

Acknowledgements

This work was supported by the National Natural Science Foundation of China (51202040, 21363006, 21503051), Guangxi Natural Science Foundation (2013GXNSFBA019042, 2012GXNSFBA053032), Scientific Research Projects of Guangxi Education (YB2014161) and Guilin Scientific Research and Technology Development Projects (KY2015ZL109)

Notes and references

1. N. Zhang, Y. Zhang and Y.-J. Xu, *Nanoscale*, 2012, **4**, 5792-5813.
2. Y. Liu, L. Fang, H. Lu, Y. Li, C. Hu and H. Yu, *Applied Catalysis B: Environmental*, 2012, **115–116**, 245-252.
3. Y. Liu, L. Fang, H. Lu, L. Liu, H. Wang and C. Hu, *Catalysis Communications*, 2012, **17**, 200-204.
4. X. Wang, K. Maeda, A. Thomas, K. Takanabe, G. Xin, J. M. Carlsson, K. Domen and M. Antonietti, *Nat Mater*, 2009, **8**, 76-80.
5. X. Wang, K. Maeda, X. Chen, K. Takanabe, K. Domen, Y. Hou, X. Fu and M. Antonietti, *Journal of the American Chemical Society*, 2009, **131**, 1680-1681.
6. S. C. Yan, Z. S. Li and Z. G. Zou, *Langmuir*, 2009, **25**, 10397-10401.
7. S. Yang, Y. Gong, J. Zhang, L. Zhan, L. Ma, Z. Fang, R. Vajtai, X. Wang and P. M. Ajayan, *Advanced Materials*, 2013, **25**, 2452-2456.
8. X. Zhang, X. Xie, H. Wang, J. Zhang, B. Pan and Y. Xie, *Journal of the American Chemical Society*, 2012, **135**, 18-21.
9. L. Chen, D. Huang, S. Ren, T. Dong, Y. Chi and G. Chen, *Nanoscale*, 2013, **5**, 225-230.
10. S. Bai, X. Wang, C. Hu, M. Xie, J. Jiang and Y. Xiong, *Chemical Communications*, 2014, **50**, 6094-6097.
11. P. Niu, L. Zhang, G. Liu and H.-M. Cheng, *Advanced Functional Materials*, 2012, **22**, 4763-4770.
12. H. Zhao, H. Yu, X. Quan, S. Chen, H. Zhao and H. Wang, *RSC Advances*, 2014, **4**, 624-628.
13. Z. Lin and X. Wang, *Angewandte Chemie International Edition*, 2013, **52**, 1735-1738.
14. J. Zhang, M. Zhang, G. Zhang and X. Wang, *ACS Catalysis*, 2012, **2**, 940-948.
15. Y. Wang, R. Shi, J. Lin and Y. Zhu, *Energy & Environmental Science*, 2011, **4**, 2922-2929.
16. Y. Wang, X. Bai, C. Pan, J. He and Y. Zhu, *Journal of Materials Chemistry*, 2012, **22**, 11568-11573.
17. H. Yan and H. Yang, *Journal of Alloys and Compounds*, 2011, **509**, L26-L29.
18. X. Xu, G. Liu, C. Randorn and J. T. S. Irvine, *International Journal of Hydrogen Energy*, 2011, **36**, 13501-13507.
19. Y. Hou, Z. Wen, S. Cui, X. Guo and J. Chen, *Advanced Materials*, 2013, **25**, 6291-6297.
20. Z. Chen, P. Sun, B. Fan, Z. Zhang and X. Fang, *The Journal of Physical Chemistry C*, 2014, **118**, 7801-7807.
21. Y.-S. Jun, J. Park, S. U. Lee, A. Thomas, W. H. Hong and G. D. Stucky, *Angewandte Chemie*, 2013, **125**, 11289-11293.
22. J. N. Coleman, M. Lotya, A. O'Neill, S. D. Bergin, P. J. King, U. Khan, K. Young, A. Gaucher, S. De, R. J. Smith, I. V. Shvets, S. K. Arora, G. Stanton, H.-Y. Kim, K. Lee, G. T. Kim, G. S. Duesberg, T. Hallam, J. J. Boland, J. J. Wang, J. F. Donegan, J. C. Grunlan, G. Moriarty, A. Shmeliov, R. J. Nicholls, J. M. Perkins, E. M. Grieveson, K. Theuwissen, D. W. McComb, P. D. Nellist and V. Nicolosi, *Science*, 2011, **331**, 568-571.
23. Y. Yao, Z. Lin, Z. Li, X. Song, K.-S. Moon and C.-p. Wong, *Journal of Materials Chemistry*, 2012, **22**, 13494-13499.
24. G. Cunningham, M. Lotya, C. S. Cucinotta, S. Sanvito, S. D. Bergin, R. Menzel, M. S. P. Shaffer and J. N. Coleman, *ACS Nano*, 2012, **6**, 3468-3480.
25. Q. Guo, Y. Xie, X. Wang, S. Lv, T. Hou and X. Liu, *Chemical Physics Letters*, 2003, **380**, 84-87.

26. M. J. Bojdys, J.-O. Müller, M. Antonietti and A. Thomas, *Chemistry – A European Journal*, 2008, **14**, 8177-8182.
27. F. Chang, C. Li, J. Chen, J. Wang, J. Luo, Y. Xie, B. Deng and X. Hu, *Superlattices and Microstructures*, 2014, **76**, 90-104.
28. G. Kiruthigaa, C. Manoharan, C. Raju, J. Jayabharathi and S. Dhanapandian, *Spectrochimica Acta Part A: Molecular and Biomolecular Spectroscopy*, 2014, **129**, 415-420.
29. J. Mao, T. Peng, X. Zhang, K. Li, L. Ye and L. Zan, *Catalysis Science & Technology*, 2013, **3**, 1253-1260.
30. J. Liu, Y. Liu, N. Liu, Y. Han, X. Zhang, H. Huang, Y. Lifshitz, S.-T. Lee, J. Zhong and Z. Kang, *Science*, 2015, **347**, 970-974.
31. V. N. Khabashesku, J. L. Zimmerman and J. L. Margrave, *Chemistry of Materials*, 2000, **12**, 3264-3270.
32. Y. Bai , X. Zong , H. Yu, Z.-G. Chen and L. Wang, *Chemistry – A European Journal*, 2014, **20**, 8670-8676.
33. T. Y. Ma, S. Dai, M. Jaroniec and S. Z. Qiao, *Angewandte Chemie International Edition*, 2014, **53**, 7281-7285.
34. J. Tian, Q. Liu, A. M. Asiri, A. O. Al-Youbi and X. Sun, *Analytical Chemistry*, 2013, **85**, 5595-5599.
35. S. Cao and J. Yu, *The Journal of Physical Chemistry Letters*, 2014, **5**, 2101-2107.
36. S.-W. Cao, X.-F. Liu, Y.-P. Yuan, Z.-Y. Zhang, Y.-S. Liao, J. Fang, S. C. J. Loo, T. C. Sum and C. Xue, *Applied Catalysis B: Environmental*, 2014, **147**, 940-946.
37. J. Yu, G. Dai and B. Huang, *The Journal of Physical Chemistry C*, 2009, **113**, 16394-16401.
38. M. A. Butler, *Journal of Applied Physics*, 1977, **48**, 1914-1920.
39. S. Chen, Y. Hu, S. Meng and X. Fu, *Applied Catalysis B: Environmental*, 2014, **150–151**, 564-573.
40. Z. Zhang, C. Shao, X. Li, Y. Sun, M. Zhang, J. Mu, P. Zhang, Z. Guo and Y. Liu, *Nanoscale*, 2013, **5**, 606-618.
41. Y. C. Zhang, Z. N. Du, K. W. Li, M. Zhang and D. D. Dionysiou, *ACS Applied Materials & Interfaces*, 2011, **3**, 1528-1537.
42. Y. C. Zhang, Z. N. Du, S. Y. Li and M. Zhang, *Applied Catalysis B: Environmental*, 2010, **95**, 153-159.
43. C. Yang, W. Wang, Z. Shan and F. Huang, *Journal of Solid State Chemistry*, 2009, **182**, 807-812.
44. K. C. Christoforidis, A. Sengele, V. Keller and N. Keller, *ACS Applied Materials & Interfaces*, 2015, **7**, 19324-19334.
45. P. Madhusudan, J. Ran, J. Zhang, J. Yu and G. Liu, *Applied Catalysis B: Environmental*, 2011, **110**, 286-295.
46. X. Lin, J. Xing, W. Wang, Z. Shan, F. Xu and F. Huang, *The Journal of Physical Chemistry C*, 2007, **111**, 18288-18293.
47. X. Chen, B. Zhou, S. Yang, H. Wu, Y. Wu, L. Wu, J. Pan and X. Xiong, *RSC Advances*, 2015, **5**, 68953-68963.
48. C. Chen, W. Ma and J. Zhao, *Chemical Society Reviews*, 2010, **39**, 4206-4219.
49. H. Li, Y. Sun, B. Cai, S. Gan, D. Han, L. Niu and T. Wu, *Applied Catalysis B: Environmental*, 2015, **170–171**, 206-214.
50. Z. Jiang, F. Yang, G. Yang, L. Kong, M. O. Jones, T. Xiao and P. P. Edwards, *Journal of Photochemistry and Photobiology A: Chemistry*, 2010, **212**, 8-13.
51. F. Duan, Y. Zheng and M. Chen, *Applied Surface Science*, 2011, **257**, 1972-1978.
52. Z. W. Tong, D. Yang, Y. Y. Sun and Z. Y. Jiang, *RSC Advances*, 2015, **5**, 56913-56921.

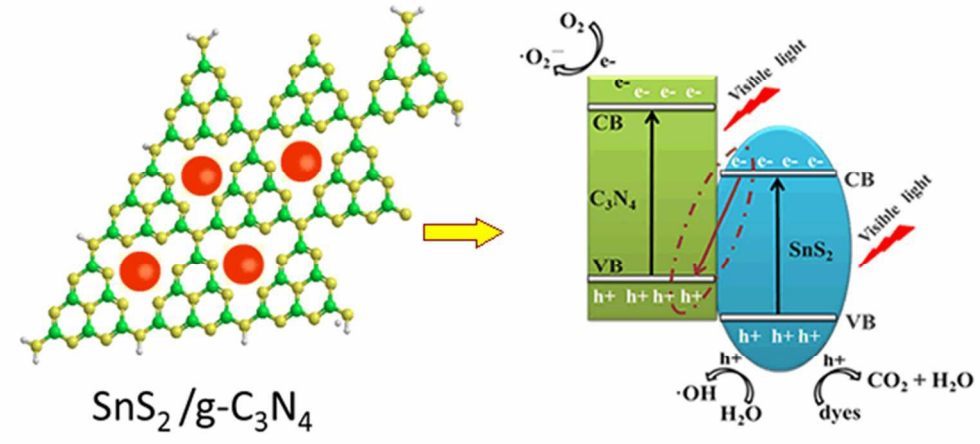

110x50mm (149 x 149 DPI)